AGU100 ADVANCING EARTH AND SPACE SCIENCE

JGR

Journal of Geophysical Research: Solid Earth

RESEARCH ARTICLE

10.1029/2018JB015545

Key Points:

- The seismic coupling coefficient for ridge normal faults scales with downdip seismogenic zone width W and critical nucleation length h^*
- Models suggest that the relatively short along-strike length of normal faults reduces seismic coupling for large W/h^*
- Moment release rates for mid-ocean ridges are best modeled with h^*~1 km and ~95% of plate separation accommodated by magma emplacement

Supporting Information:

- Supporting Information S1
- Table S1

Correspondence to:
H. F. Mark,
hmark@whoi.edu

Citation:
Mark, H. F., Behn, M. D., Olive, J.-A., & Liu, Y. (2018). Controls on mid-ocean ridge normal fault seismicity across spreading rates from rate-and-state friction models. *Journal of Geophysical Research: Solid Earth*, *123*, 6719–6733. https://doi.org/10.1029/2018JB015545

Received 23 JAN 2018
Accepted 20 JUL 2018
Accepted article online 27 JUL 2018
Published online 16 AUG 2018

Controls on Mid-ocean Ridge Normal Fault Seismicity Across Spreading Rates From Rate-and-State Friction Models

Hannah F. Mark[1,2], Mark D. Behn[2], Jean-Arthur Olive[3], and Yajing Liu[4]

[1]MIT/WHOI Joint Program in Oceanography/Applied Ocean Science and Engineering, Woods Hole, MA, USA, [2]Department of Geology and Geophysics, Woods Hole Oceanographic Institution, Woods Hole, MA, USA, [3]Laboratoire de Géologie, Ecole Normale Supérieure/CNRS UMR 8538, PSL Research University, Paris, France, [4]Department of Earth and Planetary Sciences, McGill University, Montreal, Quebec, Canada

Abstract Recent seismic and geodetic observations have led to a growing realization that a significant amount of fault slip at plate boundaries occurs aseismically and that the amount of aseismic slip varies across tectonic settings. Seismic moment release rates measured along the fast-spreading East Pacific Rise suggest that the majority of fault slip occurs aseismically. By contrast, at the slow-spreading Mid-Atlantic Ridge seismic slip may represent up to 60% of total fault displacement. In this study, we use rate-and-state friction models to quantify the seismic coupling coefficient, defined as the fraction of total fault slip that occurs seismically, on mid-ocean ridge normal faults and investigate controls on fault behavior that might produce variations in coupling observed at oceanic spreading centers. We find that the seismic coupling coefficient scales with the ratio of the downdip width of the seismogenic area (W) to the critical earthquake nucleation size (h^*). At mid-ocean ridges, W is expected to increase with decreasing spreading rate. Thus, the relationship between seismic coupling and W/h^* predicted from our models explains the first-order variations in seismic coupling coefficient as a function of spreading rate.

1. Introduction

Seismic and geodetic measurements over the last decade have revealed that plate boundary strain can be accommodated by a spectrum of fault slip behavior (e.g., Miller et al., 2002; Peng & Gomberg, 2010; Wech et al., 2009). While earthquakes are the most dramatic end member of that spectrum, it has become increasingly clear that aseismic slip over a variety of timescales contributes significantly to total fault displacement in some tectonic settings (e.g., Bird et al., 2002; Dragert et al., 2001; Frohlich & Wetzel, 2007; Schwartz & Rokosky, 2007; Sobolev & Rundquist, 1999; Vidale & Houston, 2012). Understanding the partitioning of seismic versus aseismic displacement on faults is important from a hazards perspective, as unquantified aseismic slip adds uncertainty to risk assessments for faults with the potential to generate large earthquakes (e.g., Dixon et al., 2014; Linde et al., 1996; Linde & Silver, 1989). Further, some studies suggest that aseismic slip events can trigger large earthquakes (e.g., Kato et al., 2012; Radiguet et al., 2016; Segall et al., 2006).

Compiled observations from a range of plate boundaries have been used to show that the proportion of seismic versus aseismic fault slip varies across settings (e.g., Bird & Kagan, 2004; Frohlich & Wetzel, 2007; Sobolev & Rundquist, 1999). Variable slip modes have been observed and modeled for crustal faults, in particular for convergent (e.g., Houston et al., 2011; Liu & Rice, 2005, 2007; Miller et al., 2002; Wech et al., 2009) and transform plate boundaries (e.g., Brune et al., 1969; Froment et al., 2014; Johnson et al., 2006; Linde et al., 1996; Liu et al., 2012; McGuire, 2008; McGuire et al., 2005, 2012; Roland et al., 2012).

Several studies have also addressed seismic behavior and the potential for aseismic slip on faults at divergent plate boundaries (e.g., Biemiller & Lavier, 2017; Calais et al., 2008; Cowie et al., 1993; Olive & Escartín, 2016; Sobolev & Rundquist, 1999). Observations support a range of behavior from seismic and aseismic fault slip across different ridges and ridge segments (Cowie et al., 1993; Olive & Escartín, 2016). However, interpretation of these variations has been limited due to the lack of quantitative models for seismic cycles on mid-ocean ridge normal faults.

The partitioning of fault slip can be described in a time-average sense by the seismic coupling coefficient, χ, which we define as the fraction of fault slip that occurs seismically. The seismic coupling coefficient can be estimated directly by measuring fault displacement and comparing the moment release predicted for this displacement to the observed seismic moment release (e.g., Cowie et al., 1993). However, this method is

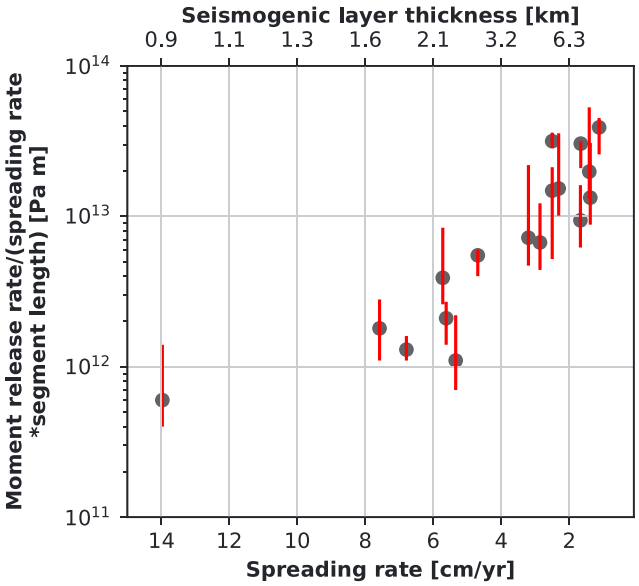

Figure 1. Seismic moment release rate at divergent plate boundaries normalized by boundary length and spreading rate (a proxy proportional to the seismic coupling coefficient; Frohlich & Wetzel, 2007; Olive & Escartín, 2016), plotted against spreading rate and seismogenic layer thickness. Seismogenic layer thickness estimated from the on-axis depth of the 600 °C isotherm as predicted by the model of Montési and Behn (2007). See section 4 for details.

labor intensive, requires high-resolution topographic maps of large areas, and may be skewed by mass-wasting processes and erosion of seafloor fault relief (e.g., Cannat et al., 2013; Goff & Tucholke, 1997). Thus, in practice, coupling is often estimated by comparing seismic moment release rates with estimates of the long-term accumulation of slip on a fault from geodetic data or tectonic reconstructions.

Seismic coupling is observed to vary across convergent (e.g., Frohlich & Wetzel, 2007; Pacheco et al., 1993; Scholz & Campos, 2012; Tichelaar & Ruff, 1993) and transform boundaries (e.g., Boettcher & Jordan, 2004; Frohlich & Wetzel, 2007; Rundquist & Sobolev, 2002) and can vary between different subduction zones, from χ = 0.1 (mostly aseismic) to 1.0 (fully coupled; e.g., Scholz & Campos, 2012). Coupling also varies between 0 and 1 along strike in individual subduction zones, over length scales of 200–600 km (Métois et al., 2012; Pacheco et al., 1993; Scholz & Campos, 2012). For transform boundaries, Frohlich and Wetzel (2007) found a systematic decrease in the seismic coupling coefficient with relative plate velocity, from ≥0.4 to ~0. By contrast, Boettcher and Jordan (2004) showed that for a global data set of 65 mid-ocean ridge transform faults with slip rates from 15 to 150 mm/year, the coupling coefficient was roughly constant at 0.15.

Several hypotheses have been proposed to explain variations in seismic coupling. One class of models argues that thermal structure and fault geometry exert the primary control on seismic coupling (Boettcher et al., 2007; Liu et al., 2012; Solomon et al., 1988). Together these two factors control the size of the seismogenic zone, defined as the area where earthquakes are able to nucleate (e.g., Scholz, 1998). Other studies, citing experimental evidence that the frictional properties of hydrous minerals such as serpentine differ significantly from those of their anhydrous counterparts (Escartín et al., 1997; Hirth & Guillot, 2013; Reinen et al., 1991, 1994), have proposed that fault zone material properties and/or heterogeneities associated with hydrous alteration or pore pressure exert a primary control on seismic coupling by enabling the nucleation of aseismic slip transients (Liu & Rice, 2005, 2007; McGuire et al., 2012; Roland et al., 2012). It has also been suggested that the magnitude of the normal force acting on the subduction interface controls seismic coupling on megathrusts (Scholz & Campos, 1995, 2012).

A compilation of the available data sets from mid-ocean ridges shows that the seismic coupling coefficient on oceanic normal faults varies inversely with spreading rate (Figure 1). Cowie et al. (1993) found the coupling coefficient for faults bounding the fast-spreading East Pacific Rise to be less than 0.01. By contrast, estimates derived using teleseismic and hydroacoustic data from the slow-spreading Mid-Atlantic Ridge indicate coupling coefficients of 0.1–0.3 for symmetric ridge segments and 0.4–0.6 for segments characterized by the presence of large-offset detachment faults (Olive & Escartín, 2016). Frohlich and Wetzel (2007) found a similar systematic variation in the coupling coefficient across a range of spreading rates using teleseismic moment release rates. Moreover, the variation in coupling with spreading rate appears to be robust even with the uncertainty introduced by assumptions regarding fault geometry and magmatism (Olive & Escartín, 2016). Several of these studies suggested that variations in fault thermal structure and the size of the seismogenic zone are responsible for the range of seismic coupling coefficients observed across different ridge spreading rates (Cowie et al., 1993; Solomon et al., 1988). However, they did not address the specific reason why faults near fast-spreading mid-ocean ridges may be more prone to slipping aseismically when they are also known to occasionally generate moderately large earthquakes (e.g., M_w~5–6 along the East Pacific Rise, Ekström et al., 2012). To date, tests of such hypotheses (e.g., Olive & Escartín, 2016) have relied on extrapolation of rate-and-state models for strike-slip faults (e.g., Liu et al., 2012) to normal fault systems, thus precluding a quantitative assessment of the effects of normal fault geometry on seismic coupling.

In this study, we examine the effects of steady state thermal structure, spreading rate, and fault geometry on the seismic coupling coefficient for mid-ocean ridge normal faults by using rate-and-state friction models to simulate fault slip on seismic cycle time scales. These new models provide a framework for interpreting

Table 1
List of Model Parameters and Their Values or Ranges

Variable	Meaning	Value/units
V_{pl}	Plate rate	25–75 mm/year
$\frac{dT}{dz}$	Vertical thermal gradient	45–127 °C/km
φ	Fault dip	25–70°
L	Along-strike fault length	25–50 km
D_C	Critical slip distance	3–18 mm
W	Downdip width of seismogenic zone	4.5–11.5 km
h^*	Critical earthquake nucleation length scale	1.0–6.6 km
μ	Shear modulus	30 GPa
$(a-b)$	Friction parameter	−0.004–0.015, dimensionless
c	Shear wave speed	3.044 km/s
η	Viscous damping factor	$\mu/2c$

observations from mid-ocean ridges. We show that seismic coupling varies systematically with the ratio of the seismogenic layer thickness to the characteristic nucleation size. Based on a comparison of our numerical results to natural systems, we argue that lithologic variations are not required to explain the variability in seismic coupling with spreading rate at mid-ocean ridges and that seismogenic layer thickness, together with the fraction of extension accommodated by magma intrusion, is the primary control on seismic behavior of oceanic normal faults.

2. Modeling Seismic Cycles on Normal Faults

Laboratory experiments have shown that the frictional resistance on an interface depends on the slip velocity during sliding, the *rate*; and on the history of slip on the surface, the *state* (e.g., Dieterich, 1972, 1978, 1979; Marone, 1998; Rice, 1993; Rice & Ruina, 1983; Ruina, 1983). The rate effect is seen during abrupt velocity changes, where friction increases or decreases proportionally to the velocity steps. When sliding velocity is not changing or the fault remains stationary, the dynamic friction varies according to the amount of time static contact is maintained under a load (Beeler et al., 1994; Dieterich, 1978). This rate-and-state frictional behavior can be quantified as a law relating shear and normal stress through a friction coefficient that depends on slip velocity and an empirical state variable θ. The formulation is closed through a second law that describes the time evolution of θ (Dieterich, 1972, 1978, 1979; Marone, 1998; Rice, 1993).

In this study, we use a single state variable friction law:

$$\tau = \overline{\sigma}\left[f_0 + a\ln\left(\frac{V}{V_0}\right) + b\ln\left(\frac{V_o\theta}{D_c}\right)\right] \tag{1}$$

Here $\overline{\sigma}$ is the effective normal stress given by $\overline{\sigma} = \sigma - p$ where p is the pore pressure, f_0 is a reference friction coefficient corresponding to a reference slip velocity V_0 at steady state (Ruina, 1983), and D_c is the critical slip distance (Table 1). From a physical perspective, rate-and-state friction describes how asperity contacts on a fault surface evolve over time; D_c represents the characteristic length scale over which a population of contacts on an interface changes from one steady state to another during sliding. The parameters a and b are temperature- and pressure-dependent properties of the material. In steady state, the derivative of the rate-and-state friction coefficient with respect to velocity is proportional to $(a-b)$ (e.g., Scholz, 1998). When $(a-b) < 0$, small increases in slip velocity will result in a drop in the friction coefficient and slip will accelerate. This behavior is referred to as *velocity weakening*. On the other hand, when $(a-b) > 0$, an increase in slip velocity will result in an increase in the friction coefficient, leading to a negative feedback on slip behavior known as *velocity strengthening*. Slip instabilities (earthquakes) nucleate in velocity-weakening areas. Values of $(a-b)$ have been measured in the lab for some materials and conditions (e.g., Blanpied et al., 1995; He et al., 2007). Assuming a typical geotherm, the $(a-b)$ profile for a typical crustal fault is characterized by a shallow region of velocity-strengthening material above a velocity-weakening zone where earthquakes nucleate. At greater depths the fault transitions back to velocity strengthening as temperature and pressure increase (Scholz, 1998). Here we refer to the velocity-weakening region as the seismogenic zone.

In our simulations, a regularized version of the friction law is used when $V < 0.001$ mm/year:

$$\tau = a\overline{\sigma}\sinh^{-1}\left[\frac{V}{2V_0}\exp\left(\frac{f_0 + b\ln(V_0\theta/D_c)}{a}\right)\right] \tag{2}$$

Equation (2) can be derived by solving equation (1) for V and replacing the factor $\exp(\tau/a\overline{\sigma})$ with $[\exp(\tau/a\overline{\sigma}) - \exp(-\tau/a\overline{\sigma})]$ to account for the possibility of backward slip when the slip velocity slows to near 0 (Ben-Zion & Rice, 1997; Lapusta et al., 2000; Rice & Ben-Zion, 1996). The regularized law in equation (2) avoids the singularity at $V = 0$ that occurs in the full friction law.

The critical slip distance D_c is directly related to the critical earthquake nucleation size h^*, which is the minimum length scale that must fail in order for a slip instability to occur. Rate-and-state models with h^* smaller than the dimensions of a grid cell will produce spurious results as single cells can generate instabilities independently of one another. To properly simulate stick-slip behavior, the model requires a critical nucleation size larger than a single cell. This is done by setting h^* to be sufficiently large relative to the model grid size and then relating h^* to D_c through the expression.

$$h^* = \frac{2\mu b D_c}{\pi(b-a)^2\bar{\sigma}} \tag{3}$$

where μ is the shear modulus (Rubin & Ampuero, 2005).

During steady state sliding, the state variable θ can be thought of as the average contact time of asperities on the interface (Dieterich, 1979; Ruina, 1983). This intuitive definition points to two main effects on the time evolution of θ. The first is the slip velocity, which has a direct effect on how long asperities remain in contact. The second is the duration of periods of no slip, referred to in lab experiments as hold periods, during which recrystallization and fault healing can occur. Expressions for the time rate of change of θ can be formulated in different ways to emphasize one or the other of these effects. Here we follow Liu et al. (2012) and employ the aging law for our calculations. The aging law, defined as

$$\frac{\mathrm{d}\theta}{\mathrm{d}t} = 1 - \frac{\theta V}{D_c} \tag{4}$$

retains the time dependence of state variable evolution (Beeler et al., 1994; Dieterich, 1978, 1979; Marone, 1998). This allows friction to evolve on stationary contacts as is observed in laboratory experiments, as well as during sliding. Setting the left-hand side of equation (4) to 0, it can be seen that the steady state value of the state variable is $\theta_{ss} = D_c/V$.

The model couples the rate-and-state friction law and state variable evolution with quasi-static elasticity, in order to quantify the effect of slip on the spatial and temporal distribution of shear stress on the fault:

$$\tau(x,\xi,t) = \int_{-L/2}^{L/2}\int_0^D k\left(x-x',\xi,\xi'\right)\left[\delta\left(x',\xi',t\right) - V_{pl}t\right]\mathrm{d}x'\,d\xi' - \eta\frac{\partial\delta(x,\xi,t)}{\partial t} \tag{5}$$

Here τ is the shear stress, x and ξ are distance measured along-strike and downdip on the fault plane, t is time, δ is slip distance, V_{pl} is the plate velocity or forcing velocity, L is the along-strike dimension of the fault, η is a viscous damping factor, and k is the stiffness kernel which we obtain from closed-form solutions (Okada, 1992) based on the fault geometry. The two terms on the right-hand side of equation (5) describe the quasi-static equilibrium connection between shear stress and slip, and the effects of viscous damping at very high slip rates, respectively. The damping term can be thought of as the energy dissipated by seismic waves. The damping factor η is chosen to be $\mu/2c$, where μ is the shear modulus and c is the shear wave speed. This value of η ensures that the slip velocity is bounded by a value on the order of $c\Delta\tau/\mu$ where $\Delta\tau$ is an average stress drop for a slip instability (Lapusta & Liu, 2009; Rice, 1993). The double integral term in equation (5) is an approximation to the full elastodynamic response and does not reproduce wave propagation effects along the fault during a slip instability. In the exact solution the product of stiffness k and slip δ would be a convolution in time to account for the finite velocity at which stress alterations due to slip propagate along the fault. Using the quasi-static approximation communicates those stress changes along the fault instantaneously to avoid the computational expense of the time convolution. Therefore, although it cannot be used to model dynamic rupture processes, this approach provides a good approximation for timescales covering several earthquake cycles (Lapusta & Liu, 2009).

To simulate slip on a two-dimensional fault plane, we use a boundary integral approach to calculate the evolution of slip velocity through time. Differentiating the friction law and the quasi-static elastic relation gives two equations for the time derivative of τ, which can be equated and solved to find the time derivative of the slip velocity. The fault surface is discretized into rectangular grid cells with the slip velocity V and state variable θ specified in each cell. The discretized stiffness kernel is calculated for each grid cell using closed-form solutions for shear displacement on a fault plane in an elastic half-space (Okada, 1992). For a plate

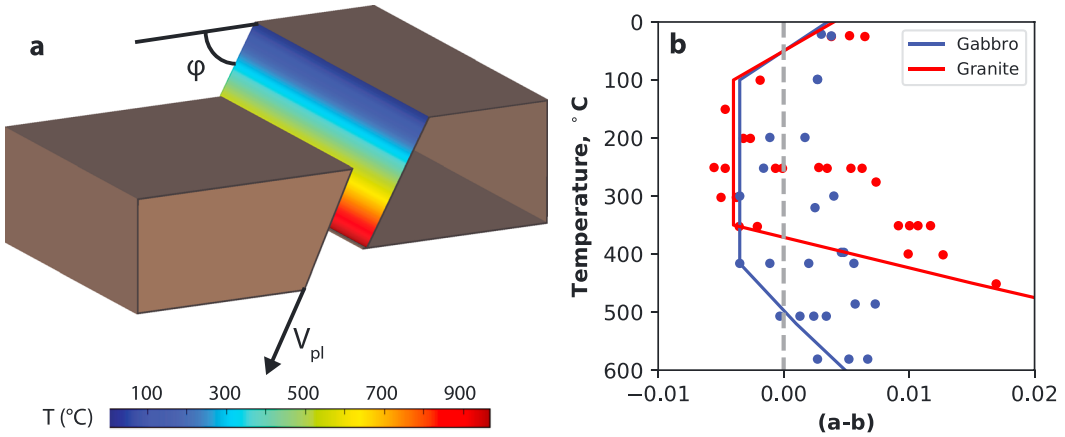

Figure 2. (a) Three-dimensional schematic diagram of the model setup showing fault dip (φ), imposed slip velocity at the base of the fault (V_{pl}), and temperature on the fault plane. (b) Frictional parameter ($a - b$) for gabbro (blue) and granite (red) are shown as a function of temperature. Dots show data from laboratory experiments (Blanpied et al., 1995; He et al., 2007); curves show simplified fits to these data used in our simulations. The scatter in the data at each temperature is due to experimental runs at different normal stress conditions and/or different size steps for velocity increases or decreases.

rate V_{pl} we impose an initial slip velocity V_0 as the portion of the horizontal plate velocity resolved on the fault surface and set the initial state variable to a value slightly out of steady state at $\theta_0 = D_c/(1.1 * V_0)$. The model then evolves both quantities in time using the time derivative of velocity and the aging law for state variable evolution given by equation (4) (Beeler et al., 1994; Rice, 1993; Ruina, 1983). The model steps forward in time using a fifth-order Cash-Karp Runge-Kutta method with an adaptive stepsize control (Cash & Karp, 1990).

For each simulation we specify the thermal gradient, fault dip, forcing velocity, and along-strike fault length (Figure 2 and supporting information Table S1). The friction parameter ($a - b$) is mapped onto the fault surface based on the imposed temperature structure, using relationships from laboratory data for either granite or gabbro (Blanpied et al., 1995; He et al., 2007).

We use the modeled cumulative fault slip to calculate the seismic coupling coefficient for each simulation. The coupling coefficient is determined from the ratio of seismic slip (defined when the slip velocity exceeds the threshold velocity) to the total fault slip (defined as plate rate times the total elapsed time). We excluded slip near the edges of faults because edge effects tend to suppress slip close to the boundaries. We found that running simulations for 300 years allowed sufficient time for the coupling coefficient to converge to a stable value. The coupling coefficient for each simulation is taken to be the value at the end of the run, and the uncertainty in the coupling coefficient is estimated from the range of values over the run excluding the first simulated earthquake, which induces a large jump in coupling coefficient as the system adjusts to the initial conditions (see Liu et al., 2012, Figure 3; Table S1).

3. Rate-and-State Model Results

In our simulations, the imposed thermal gradient (Figure 2a) determines the distribution of the friction parameter ($a - b$), which in turn sets the downdip width of the seismogenic zone (W; Figures 2b, 3a, and 3e). Figure 3 compares the general behavior of a simulation case with large W (Figures 3a–3d) versus a case with moderate W (Figures 3e–3h). At each time step, we calculate the maximum slip velocity on the fault (Figures 3c and 3g). Slip instabilities are easily identified as sharp spikes in the maximum velocity time series. The model also calculates the cumulative distance that the fault has slipped, averaged over the seismogenic zone. Cumulative slip is tracked at regular time intervals to capture the progress of interseismic slip. Slip is also tracked when the maximum slip rate exceeds a given velocity threshold to capture coseismic slip (Figures 3b and 3f). To test the sensitivity of our results to the assumed threshold velocity, we tracked coseismic slip using two threshold velocities of 1 and 5 mm/s.

For the case with $W = 9.1$ km, earthquakes occur across almost the entire width of the fault at regular intervals (Figures 3b and 3c). By contrast, when $W = 5.7$ km, earthquakes occur at irregular intervals and do not rupture

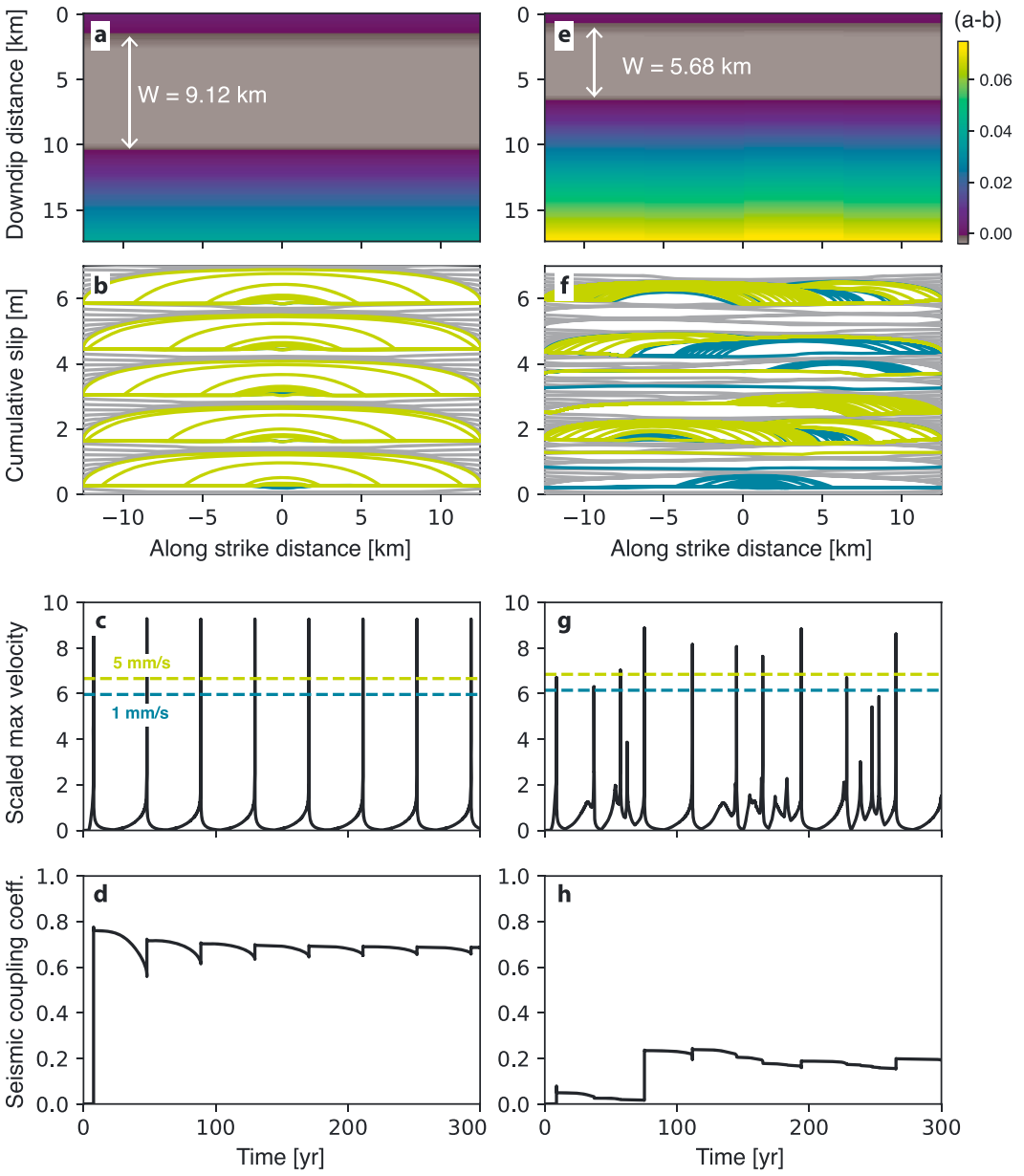

Figure 3. Model results for two simulations, with W = 9.1 km (*d40t55hs10*, a–d) and W = 5.7 km (*u1hs12*, e–h). Both simulations use h^* ~3.5 km and V_{pl} = 4.5 cm/year. (a, e) Imposed distribution of $(a - b)$ on the fault surface. (b, f) Cumulative slip contours averaged over the seismogenic zone. Gray lines show interseismic slip, contoured at 5-year intervals. Blue lines show slip at velocities >1 mm/s, contoured at 200-s intervals. Green lines show slip at velocities >5 mm/s, contoured at 15-s intervals. (c, g) Log of maximum slip velocity scaled by the plate rate, as a function of time. (d, h) Seismic coupling coefficient through time.

all the way across the fault (Figures 3f and 3g). We quantify the differences between the two simulations by calculating the ratio of the cumulative seismic slip to the total slip throughout each simulation, averaged over the seismogenic zone (Figures 3d and 3h). The coupling coefficient decreases slowly during interseismic periods and increases abruptly when earthquakes occur. Over time the jumps in coupling due to earthquakes become smaller, as the cumulative total slip increases and each successive event has a smaller effect on the ratio. In the case with larger W, the coupling coefficient converges to a stable value of 0.69 assuming a threshold velocity of 1 mm/s (Figure 3d). For the case with smaller W, a larger fraction of the total fault slip occurs aseismically, so the coupling coefficient converges to a much lower value of

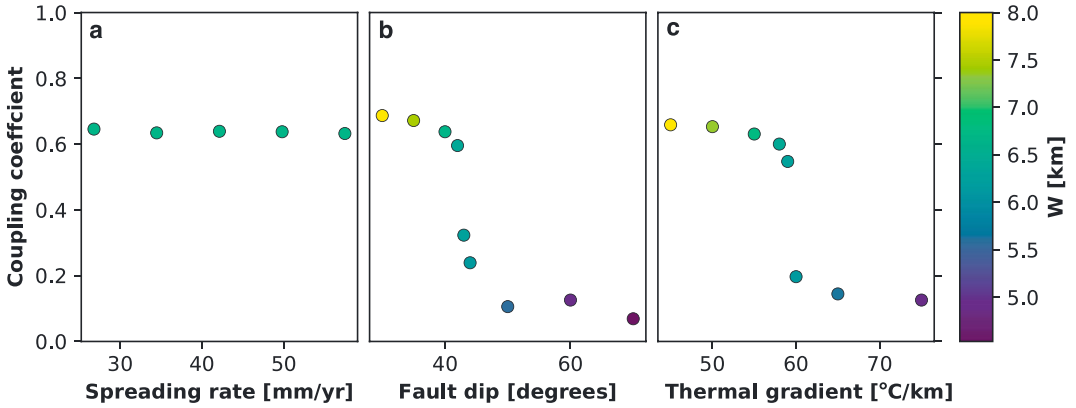

Figure 4. Calculated seismic coupling coefficient as a function of (a) spreading rate, (b) fault dip, and (c) vertical temperature gradient. h^* is ~3.6 km in all model runs, and points are colored by the width of the seismogenic zone. We find that spreading rate does not affect seismic coupling; however, coupling varies systematically with fault dip and the vertical thermal gradient. As discussed in the text, we infer that the sensitivity of the coupling coefficient to fault dip and thermal gradient is related to the influence of these parameters on the width of the seismogenic zone.

0.19 (Figure 3h). We find that these estimates are not strongly sensitive to the choice of the threshold velocity for seismic slip. For example, if we assume a threshold of 5 mm/s instead of 1 mm/s, the coupling coefficients for these two simulations decrease to 0.67 and 0.11, respectively.

We systematically investigated the effects of fault dip, thermal gradient, plate rate, and along-strike fault length on seismic coupling in the model (Figure 4 and Table S1). As anticipated, the plate rate used to drive the model does not affect the seismic coupling coefficient (Figure 4a) because it does not appear in the state variable evolution law or the rate-and-state friction law. This also demonstrates that the seismic coupling coefficient calculated at the end of each model run was not influenced by using the plate rate as the initial condition for the fault slip rate when spinning up the model. However, the earthquake recurrence interval does decrease systematically with increasing spreading rate when all other variables are held equal. This is expected because the plate rate is required to calculate the accumulated stress in equation (5).

To mimic the typical length of mid-ocean ridge normal faults, we examined along-strike fault lengths of 25–50 km and found that seismic coupling was not affected by the along-strike fault length within that range. In test cases using a much smaller along-strike dimension similar to or smaller than W, we found that very short faults ($L < W$) suppress earthquake nucleation in the model, suggesting that an equivalent characteristic nucleation length is also required for the along-strike dimension.

Variations in fault dip and the vertical thermal gradient have a pronounced influence on the coupling coefficient (Figures 4b and 4c, respectively). Specifically, when h^* is held constant coupling increases with decreasing fault dip and for colder thermal gradients. To interpret these variations, we ran an additional series of models holding spreading rate, fault dip, and the vertical thermal gradient constant and varying h^*. These simulations show that the seismic coupling coefficient increases systematically with decreasing h^*, consistent with previous results on thrust (e.g., Liu & Rice, 2007) and strike-slip (e.g., Liu et al., 2012) faults. We therefore infer that the sensitivity of seismic coupling to fault dip and thermal gradient is related to their respective roles in controlling the down-dip width of the seismogenic layer W. For constant h^*, the coupling coefficient scales with W regardless of whether W is changed by varying the thermal structure or the fault dip.

Our model results indicate that seismic coupling on normal faults is strongly controlled by the down-dip width of the seismogenic zone W relative to the critical nucleation patch size h^*. Following Liu et al. (2012), we quantify this relationship by plotting the seismic coupling coefficient χ against the dimensionless ratio W/h^* for each run (Figure 5). We completed 110 model runs in which W and h^* were varied independently by systematically changing fault dip, lithology, thermal gradient, and D_C. In all these runs, the seismic coupling coefficient was primarily sensitive to the value of W/h^* regardless of which parameter was changed (Table S1). Specifically, we find that χ goes to 0 (completely aseismic slip) for $W/h^* \leq 1.3$, jumps to ~0.7 for $W/h^* > 2$, and increases to ~0.90 when W/h^* exceeds 5.

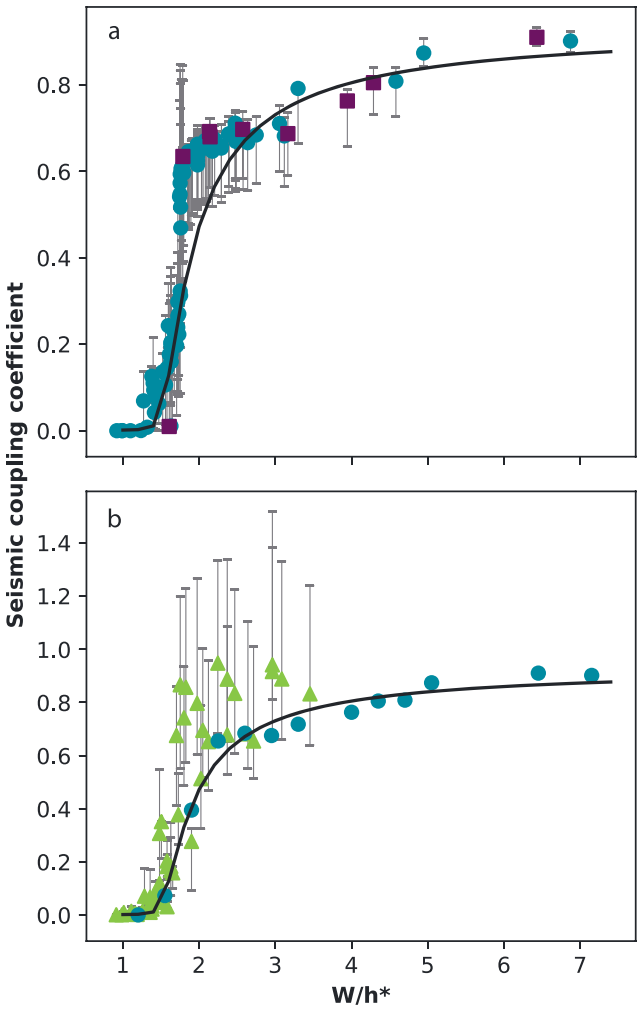

Figure 5. (a) Seismic coupling coefficient plotted against W/h^* for all model runs listed in Table S1: Purple squares correspond to runs with $(a - b)$ based on granite (Blanpied et al., 1995), and blue circles are for runs with $(a - b)$ based on gabbro (He et al., 2007). Uncertainty estimates are based on the range of coupling excluding the first slip instability of each model run. The black line shows the fit of equation (6) to the binned data points shown in (b; see section 4). (b) Results from the transform fault models of Liu et al. (2012) are plotted as green triangles, and bin averages of the points in (a) are shown by blue circles. The black line is, again, the fit to the bin averages.

There were no resolvable differences in the seismic coupling coefficient between simulations where frictional parameters were based on laboratory data from gabbro versus granite samples. Figure 5 shows that seismic coupling for both materials fall along the same trend with W/h^*. The details of the distribution of $(a - b)$ as a function of depth are slightly different for the two materials, with gabbro reaching slightly less negative values compared to granite (Figure 2b; Blanpied et al., 1995; He et al., 2007). However, in both cases the overall profile for a crustal fault goes from shallow velocity strengthening, through a velocity-weakening seismogenic zone, and back to velocity strengthening at depth. The $(a - b)$ distribution sets the value of W, and $(a - b)$ also factors into the value of h^* through equation (3); thus, the differences in frictional parameters between these two materials are reflected in W/h^*.

4. Discussion

The models presented above indicate that the seismic coupling coefficient for normal faults scales with the ratio of the width of the seismogenic layer to the critical earthquake nucleation size (W/h^*). We now contrast these model results with previous rate-and-state models of oceanic transform faults and compare our new normal fault simulations with observations from mid-ocean ridge normal faults. Finally, we extend our results to a case with much thicker lithosphere to test whether our models also apply to continental rift systems.

4.1. Comparison of Seismic Coupling in Oceanic Normal and Transform Fault Models

The scaling relationship between χ and W/h^* that we derive for normal faults is similar in form to the relationship found by Liu et al. (2012) for oceanic transform faults (Figure 5). For suites of models the seismic coupling coefficient increases abruptly over a narrow range of W/h^* values between 1 and 2. However, in the case of transform faults, Liu et al. (2012) found that the seismic coupling coefficient reached a fully coupled value of 1 for $W/h^* > 2$. By contrast, we find that normal faults do not become fully coupled for W/h^* values up to ~7.

Seismic coupling may be lower in the normal fault models because the faults we examined here are shorter in their along-strike dimension compared to the transform fault cases examined by Liu et al. (2012). To mitigate edge effects in our models, we excluded fault slip adjacent to the fault edges from the summations of cumulative moment release; however, the length of the faults may limit the total seismic moment release. The along-strike lengths of the transform fault models of Liu et al. (2012) mimicked the lengths of natural oceanic transforms, while the normal fault lengths in this study were chosen to match the observed lengths of normal fault scarps on the seafloor. The transform models with the longest faults (500 km) resulted in distinctly higher seismic coupling than the shorter transforms (100–300 km) before full coupling is reached (Liu et al., 2012). To test whether along-strike length was limiting the coupling coefficient in our models, we ran cases with 400- and 500-km-long normal faults and found that increasing the along-strike fault length resulted in seismic coupling closer to that observed in transform models with similar W/h^*. In reality, such large along-strike fault lengths are not representative of oceanic normal faults, where first- and second-order spreading segments are typically $<$100 km in length (e.g., Macdonald et al., 1991, 1992). This underscores the importance of basing quantitative interpretations of oceanic normal fault behavior on models calculated with appropriate fault geometries.

Another difference between our normal fault models and those calculated for oceanic transforms is that the normal fault models include effects due to varying fault dip on seismic coupling beyond the dependence of

W on dip. This dip effect derives from the influence of the free surface and will be more pronounced for normal faults as their average depth is less than that of a transform fault with the same value of W. However, most of our model runs were for relatively steep normal faults (<25% of the model runs used fault dips less than 50°), so free surface effects alone are unlikely to account for the difference between the normal and transform fault models.

4.2. Implications for Seismic Coupling at Mid-ocean Ridges

We quantitatively compare the predictions of our models with observations at mid-ocean ridges. To do this, we first fit the model outputs of W/h^* versus χ with the empirical function.

$$\chi = 10^{c_1 + \tan^{-1}\left(\frac{\frac{W}{h^*} - c_2}{c_3}\right)} \tag{6}$$

This functional form was chosen because it follows the shape of an asymmetric sigmoid, thereby fitting both the region of low W/h^* where χ is flat at 0 and the gradual increase in χ for large W/h^*. Equation (6) was fit to the model results with the Python package *scipy.optimize* using nonlinear least squares and a trust region minimization algorithm (Voglis & Lagaris, 2004). The individual model runs were binned before fitting because the full data set is heavily weighted toward runs with W/h^*~2. Fitting without bins favors a function with a sharp corner near W/h^*~2 at the expense of fitting runs with $W/h^* > 5$. Using this approach, we obtained optimal parameters of $c_1 = -1.60$, $c_2 = 1.46$, and $c_3 = 0.16$ (Figure 5).

To compare these estimates of coupling to data from natural systems, we use observations of moment release rate normalized by spreading rate and segment length. The coupling coefficient can be related to the normalized moment release rate $\dot{M}_0$ by

$$\chi = \frac{\dot{M}_0 \sin\varphi}{V_{pl}\mu H(1 - M)} \tag{7}$$

where H is the thickness of the seismogenic layer and M is the fraction of plate separation accommodated by magmatism (i.e., not on faults; Buck et al., 2005; Olive & Escartín, 2016). Combining equation (7) with our functional fit to the model results (equation (6)), we solve for the moment release rate as a function of seismogenic layer thickness and then explore the sensitivity of this relation to the assumed values of M and h^*. Earthquakes in the oceanic lithosphere are generally observed to occur shallower than the 600 °C isotherm (e.g., Bergman & Solomon, 1984; W.-P. Chen & Molnar, 1983; Mckenzie et al., 2005; Wiens & Stein, 1984), and the transition from velocity weakening to velocity strengthening in olivine is also thought to occur near that temperature (Boettcher et al., 2007). Thus, we relate the seismogenic layer thickness to the observed spreading rate using the thermal model of Montési and Behn (2007). Specifically, we calculate the on-axis depth to the 600 °C isotherm, assuming a high thermal diffusivity of $\kappa = 4 \times 10^{-6}$ m^2/s in order to account for the effects of hydrothermal circulation (Phipps Morgan et al., 1987; C. A. Stein & Stein, 1992).

Figure 6a shows observations from mid-ocean ridges with curves calculated using equation (7) with constant h^* and varying M. With $h^* = 1$ km, the mid-ocean ridge data are best fit by $M = 0.85$–0.95 and are ill fit by much smaller M values. Figure 6b shows the same data but with curves using constant $M = 0.95$ and varying h^*. The mid-ocean ridge data appear best fit by a value of h^*~1 km and observations for seismogenic layer thicknesses <5 km cannot be fit by $h^* >$ ~2.5 km.

A least squares fit to the observations from mid-ocean ridges gives best fit parameters of $M = 0.93$ and $h^* = 1.6$ km. The M value is roughly consistent with previous observations of seismic moment release (Solomon et al., 1988) and cumulative fault slip (Behn & Ito, 2008; Escartín et al., 1999; Howell et al., 2016), which indicate that 70–90% of plate separation at mid-ocean ridges is accommodated by magma intrusion.

The value of h^* in natural systems is a topic of some debate. Laboratory measurements of D_c predict very small h^* (D_c~10 μm, h^*~5 m; Boettcher et al., 2007), while rate-and-state models such as those used in this and other studies (e.g., Liu et al., 2012; Liu & Rice, 2007) require D_c and h^* orders of magnitude larger than the laboratory values in order to fit observations. Here we find that although an h^* of 5 m can fit observations at large seismogenic layer thickness ($H > 8 - 10$ km), the optimal value $h^* = 1.6$ km is much larger in line with

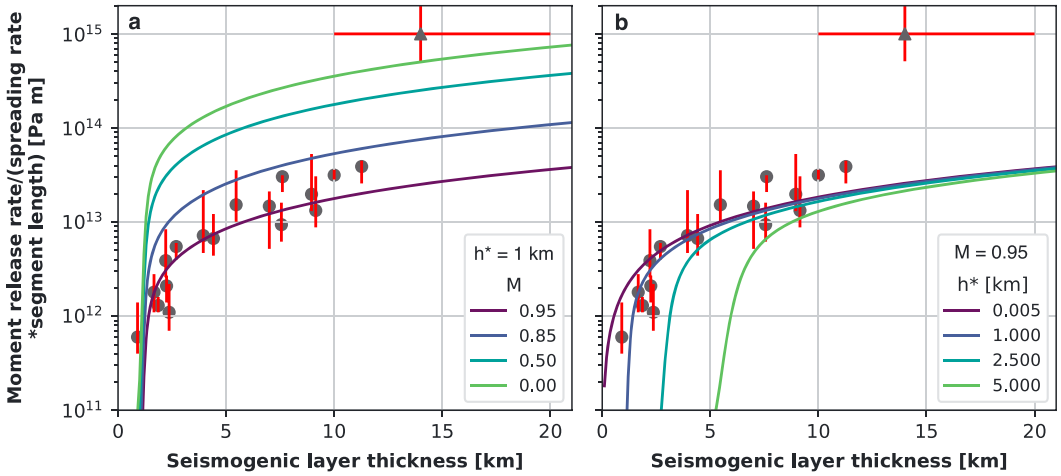

Figure 6. Observations of seismic moment release rate normalized by spreading rate and segment length versus estimated seismogenic layer thickness for mid-ocean ridges (circles; Frohlich & Wetzel, 2007; Olive & Escartín, 2016) and the Corinth rift (triangle, this study). The moment release rate for Corinth is calculated using a spreading rate of 13 mm/year and a segment length of 90–107 km. (a) Model predictions (colored lines) are calculated assuming different values of M and $h^* = 1$ km. The mid-ocean ridge data are best fit by M between 0.85 and 0.95, while the Corinth rift point falls closest to the $M = 0$ line. This is consistent with expectations for the amount of magmatic strain accommodation in these settings. (b) Model predictions (colored lines) calculated from the empirical fit in Figure 5 with $M = 0.95$ and different values of h^*. In thinner lithosphere, the data are best fit by $h^* \sim 1$ km, while in thicker lithosphere, multiple values of h^* fit the data equally well.

previous rate-and-state modeling studies. It is noteworthy that D_c may scale with gouge size (e.g., Marone & Cox, 1994), in which case laboratory measurements on small samples would not be directly applicable to much larger natural faults.

If h^* represents the minimum length scale that must fail in order to nucleate an earthquake, then h^* values on the order of kilometers pose a problem for small earthquakes. For example, with the h^* values used in our models, we cannot produce earthquakes with $M_w < 4$, which involve rupture lengths shorter than ~1 km. Some studies suggest that the nucleation length scale varies with the size of the following event (Dodge et al., 1996; Ellsworth & Beroza, 1995), while others have argued that the self-similarity of earthquake rupture processes breaks down below some threshold for small earthquakes (e.g., Jin et al., 2000). Either possibility would allow for different characteristic nucleation length scales to govern different scales of earthquakes. For example, small repeating earthquakes of $M_w < 4$ can be simulated within a velocity-weakening asperity of $h^* \sim 50$–100 m embedded in a velocity-strengthening background (T. Chen & Lapusta, 2009). In this case, seismic coupling at the scale of the asperity directly scales with the ratio of the patch size to h^*. Small events may thus be related to asperity-scale processes, while larger events could be controlled by mechanical processes averaged over many asperities. Further, h^* may vary spatially due to fault zone heterogeneity, allowing different scales of events to occur on different parts of a fault.

In summary, the value of h^* in natural systems remains a question, as models like ours do not fully agree with laboratory values. The observations are best fit by $h^* = 1.6$ km, a much larger value than has been previously obtained from laboratory experiments. Detailed studies of the source parameters of small earthquakes ($M_w < 4$) may help bridge the gap between laboratory measurements of h^* and the nucleation length scales of large faults.

An important outcome of our modeling is that the expected variations in ridge thermal structure and fault geometry are sufficient to generate the variations in seismic coupling observed at mid-ocean ridges and that material heterogeneities are not required to explain the observations. Of course, hydrous alteration and fluid circulation play an important role in fault zones, and incorporating heterogeneous materials in models can provide insight into higher-order complexities of the seismic cycle (e.g., Barbot et al., 2012). However, the fact that our model accurately predicts seismic coupling at mid-ocean ridges using a reasonable M value shows that hydrous alteration and heterogeneous fluid pressures are not required to explain first-order trends of seismic coupling across mid-ocean ridges.

4.3. Seismic Coupling in Thicker Lithosphere: Applications to Continental Rift Systems

Our model predicts that fault geometry and ridge thermal structure control seismic coupling on oceanic normal faults through their influence on the width of the seismogenic zone, in agreement with observations from mid-ocean ridges. However, the mid-ocean ridge data shown in Figure 6 are limited to relatively thin oceanic lithosphere ($H <$ ~10 km). Moreover, even at slow-spreading ridges the fraction of extension accommodated by magma is thought to be relatively high with $M > 0.7$ (Behn & Ito, 2008), with the exception of regions immediately adjacent to detachment faults (Behn & Ito, 2008; Tucholke et al., 2008), which ultimately account for a small fraction of total ridge length. Thus, to further test the applicability of our normal fault models, we must look toward data from systems with thicker lithosphere and lower magma fluxes, such as continental rifts.

Existing estimates of seismic coupling for continental rift systems are based on global averages of seismic moment release rates and are not significantly different from estimates of coupling for slow-spreading mid-ocean ridges (Bird & Kagan, 2004; Olive & Escartín, 2016). This could be due to the large uncertainty in estimates of seismic coupling for continental rifts. Globally averaged estimates of coupling in continental rifts rely on assumptions for the fault dip and thickness of the seismogenic layer. Using data from multiple rift systems involves large uncertainties on these assumptions, which in turn propagates into large uncertainty in the inferred seismic coupling coefficient. Moreover, most individual rifts lack seismic catalogs of sufficient time length to capture multiple seismic cycles, precluding estimates of seismic coupling for individual rifts.

To address these limitations, we estimated seismic coupling for the Corinth rift, a single, well-studied rift system located in the Gulf of Corinth where tighter constraints can be placed on fault dip and seismogenic layer thickness based on local structural geology and seismic data. We chose to focus on the Corinth rift because a local seismic catalog spanning 40+ years was available for analysis (Makropoulos et al., 2012), complete down to $M_L = 3.7$ (Wiemer & Wyss, 2000). Extensive information is also available on regional structure, and the distribution of seismicity suggests that the seismogenic layer is between 10 and 20 km thick (Armijo et al., 1996; Beckers et al., 2015; Bell et al., 2009; Bernard et al., 1997; Briole et al., 2000; Chouliaras et al., 1997; Clément et al., 2004; Lambotte et al., 2014; Micarelli et al., 2003; Moretti et al., 2003; Rigo et al., 1996; Taylor et al., 2011; Zelt et al., 2005). We estimated the seismic coupling coefficient for the Corinth rift using both the local catalog with moment conversions (Deichmann, 2006, 2017; Hanks & Boore, 1984; Papazachos et al., 1997), and data from the International Seismological Centre catalog (International Seismological Centre, 2017). The methods used to calculate the coupling coefficient are described in detail in the supporting information. We find that faults in the Corinth rift are likely to be fully or almost fully coupled, with a coupling coefficient of 1 ± 0.3. This is significantly different from observations at slow-spreading mid-ocean ridges where the coupling coefficients are ~0.1–0.6 (Olive & Escartín, 2016).

Predictions from our normal fault models can match the normalized moment release rate for the Corinth rift with $M = 0$, consistent with the absence of magmatic activity in this rift, and with the same approximate h^* value of 1 km as fits the mid-ocean ridge data (Figure 6a). We stress that the Corinth rift is only one example of coupling in a continental rift and cannot be used to conclude that our models apply across all divergent plate boundaries. However, it does suggest that these models may be applicable in thicker lithosphere and in settings with different time-averaged magmatic strain accommodation. As previously mentioned, it is difficult to estimate coupling in most individual rift systems because of a lack of data, but future studies should test the model predictions presented here by estimating seismic coupling in other locations where sufficient data can be found.

5. Conclusions and Perspectives

Analysis of earthquake catalogs at mid-ocean ridges reveals that the energy associated with repeated seismic ruptures falls short of the moment release expected for observed long-term slip on normal faults. This observation suggests that aseismic slip is essential to the accumulation of offset on mid-ocean ridge normal faults.

One end-member explanation is that the fault surface is mechanically heterogeneous and only hosts a few patches capable of rupturing in a seismic manner. Normal faulting earthquakes as large as $M_w \sim 5 - 6$ (typically associated with rupture lengths ~10 km) have, however, been observed at fast-spreading ridges, suggesting that the weak seismic coupling characteristic of these settings cannot be explained solely by

seismogenic slip being confined to small, isolated patches. Further, the heterogeneity model provides no straightforward explanation for why the seismic moment deficit is greater at faster-spreading mid-ocean ridges.

The alternative explanation we consider here postulates that a reduction in the size of the seismogenic zone hinders the nucleation of slip instabilities on normal faults. This favors a mixed mode of slip where normal fault growth occurs through both aseismic transients and earthquakes that repeatedly rupture the same areas. The hotter thermal regime associated with faster-spreading rates reduces the extent of the seismogenic zone, which shifts the balance toward fewer earthquakes, more aseismic transients, and lower seismic coupling. This explanation is favored by models of strike-slip and thrust faults but had not previously been tested in models with the specific geometry of normal faults.

In this study, we present a suite of normal fault models to test whether variations in the size of the seismogenic zone could produce the range of seismic coupling observed in natural systems. Our models show that this effect can account for the observed trend of seismic moment release rate versus seismogenic layer thickness (Figures 1 and 6), provided the characteristic nucleation size of earthquakes (h^*) is of order 1 km. The models fit observations from mid-ocean ridges with $M = 0.85–0.95$ and can explain observed moment release rates in the Corinth rift with $M = 0$. We find a relationship between seismic coupling and W/h^* similar to that seen in transform fault models, but the shorter length of mid-ocean ridge normal faults may limit seismic coupling for large W/h^* compared with long oceanic transforms.

While our models show that variations in the width of the seismogenic zone can explain the first-order trends in observations from mid-ocean ridges, other factors may also contribute to local variability. For example, fault behavior likely also reflects the combined effects of frictional heterogeneities, geometric complexity of the fault zone, and some degree of tectono-magmatic interaction, as well as the finite extent of the seismogenic zone. A satisfying mechanism or combination of mechanisms to explain segment-to-segment variability will need to account for not only the magnitude of the seismic deficit at mid-ocean ridges but also for the trends in seismic deficit across spreading rates. Future work building on this understanding of first-order controls on seismic coupling for normal faults can begin to target more complex controls on normal fault seismicity. Models could combine a rate-and-state framework with time-dependent magmatism to look at the effects of dike intrusions on seismic cycles. Further, seismic and geodetic observations of discrete continental rifting events from well-instrumented rift systems (e.g., Calais et al., 2008; Ebinger et al., 2010; Keir et al., 2006) can help us understand the interplay between magmatism and tectonic extension at divergent boundaries over a wider range of seismogenic layer thicknesses and M values than are found in the oceans.

Acknowledgments
Funding was provided by an NSF Graduate Research Fellowship (H. M.), NSF awards OCE-10-61203 (M. B. and Y. L.) and EAR-10-10432 (M. B.), and a WHOI IR&D award (M. B.). The data used are listed in the references and Table S1.

References

Armijo, R., Meyer, B., King, G. C. P., Rigo, A., & Papanastassiou, D. (1996). Quaternary evolution of the Corinth rift and its implications for the late Cenozoic evolution of the Aegean. *Geophysical Journal International*, *126*(1), 11–53. https://doi.org/10.1111/j.1365-246X.1996.tb05264.x

Barbot, S., Lapusta, N., & Avouac, J.-P. (2012). Under the hood of the earthquake machine: Toward predictive modeling of the seismic cycle. *Science*, *336*(6082), 707–710. https://doi.org/10.1126/science.1218796

Beckers, A., Hubert-Ferrari, A., Beck, C., Bodeux, S., Tripsanas, E., Sakellariou, D., & De Batist, M. (2015). Active faulting at the western tip of the Gulf of Corinth, Greece, from high-resolution seismic data. *Marine Geology*, *360*, 55–69. https://doi.org/10.1016/j.margeo.2014.12.003

Beeler, N. M., Tullis, T. E., & Weeks, J. D. (1994). The roles of time and displacement in the evolution effect in rock friction. *Geophysical Research Letters*, *21*(18), 1987–1990. https://doi.org/10.1029/94GL01599

Behn, M. D., & Ito, G. (2008). Magmatic and tectonic extension at mid-ocean ridges: 1. Controls on fault characteristics. *Geochemistry, Geophysics, Geosystems*, *9*, Q08010. https://doi.org/10.1029/2008GC001965

Bell, R. E., McNeill, L. C., Bull, J. M., Henstock, T. J., Collier, R. E. L., & Leeder, M. R. (2009). Fault architecture, basin structure and evolution of the Gulf of Corinth rift, central Greece. *Basin Research*, *21*(6), 824–855. https://doi.org/10.1111/j.1365-2117.2009.00401.x

Ben-Zion, Y., & Rice, J. R. (1997). Dynamic simulations of slip on a smooth fault in an elastic solid. *Journal of Geophysical Research*, *102*(B8), 17,771–17,784. https://doi.org/10.1029/97JB01341

Bergman, E. A., & Solomon, S. C. (1984). Source mechanisms of earthquakes near mid-ocean ridges from body waveform inversion: Implications for the early evolution of oceanic lithosphere. *Journal of Geophysical Research*, *89*(B13), 11,415–11,441. https://doi.org/10.1029/JB089iB13p11415

Bernard, P., Briole, P., Meyer, B., Lyon-Caen, H., Gomez, J.-M., Tiberi, C., et al. (1997). The M_s = 6.2, June 15, 1995 Aigion earthquake (Greece): Evidence for low angle normal faulting in the Corinth rift. *Journal of Seismology*, *1*(2), 131–150.

Biemiller, J., & Lavier, L. (2017). Earthquake supercycles as part of a spectrum of normal fault slip styles. *Journal of Geophysical Research: Solid Earth*, *122*, 3221–3240. https://doi.org/10.1002/2016JB013666

Bird, P., & Kagan, Y. Y. (2004). Plate-tectonic analysis of shallow seismicity: Apparent boundary width, beta, corner magnitude, coupled lithosphere thickness, and coupling in seven tectonic settings. *Bulletin of the Seismological Society of America*, *94*(6), 2380–2399. https://doi.org/10.1785/0120030107

Bird, P., Kagan, Y. Y., & Jackson, D. D. (2002). Plate tectonics and earthquake potential of spreading ridges and oceanic transform faults. In S. Stein & J. T. Freymueller (Eds.), *Plate boundary zones* (pp. 203–218). Washington, DC: American Geophysical Union. https://doi.org/10.1029/GD030p0203

Blanpied, M. L., Lockner, D. A., & Byerlee, J. D. (1995). Frictional slip of granite at hydrothermal conditions. *Journal of Geophysical Research*, *100*(B7), 13,045–13,064. https://doi.org/10.1029/95JB00862

Boettcher, M. S., Hirth, G., & Evans, B. (2007). Olivine friction at the base of oceanic seismogenic zones. *Journal of Geophysical Research*, *112*, B01205. https://doi.org/10.1029/2006JB004301

Boettcher, M. S., & Jordan, T. H. (2004). Earthquake scaling relations for mid-ocean ridge transform faults. *Journal of Geophysical Research*, *109*, B12302. https://doi.org/10.1029/2004JB003110

Briole, P., Rigo, A., Lyon-Caen, H., Ruegg, J. C., Papazissi, K., Mitsakaki, C., et al. (2000). Active deformation of the Corinth rift, Greece: Results from repeated global positioning system surveys between 1990 and 1995. *Journal of Geophysical Research*, *105*(B11), 25,605–25,625. https://doi.org/10.1029/2000JB900148

Brune, J. N., Henyey, T. L., & Roy, R. F. (1969). Heat flow, stress, and rate of slip along the San Andreas fault, California. *Journal of Geophysical Research*, *74*(15), 3821–3827. https://doi.org/10.1029/JB074i015p03821

Buck, W. R., Lavier, L. L., & Poliakov, A. N. (2005). Modes of faulting at mid-ocean ridges. *Nature*, *434*(7034), 719–723. https://doi.org/10.1038/nature03358

Calais, E., d'Oreye, N., Albaric, J., Deschamps, A., Delvaux, D., Déverchère, J., et al. (2008). Strain accommodation by slow slip and dyking in a youthful continental rift, East Africa. *Nature*, *456*(7223), 783–787. https://doi.org/10.1038/nature07478

Cannat, M., Mangeney, A., Ondréas, H., Fouquet, Y., & Normand, A. (2013). High-resolution bathymetry reveals contrasting landslide activity shaping the walls of the mid-Atlantic ridge axial valley. *Geochemistry, Geophysics, Geosystems*, *14*, 996–1011. https://doi.org/10.1002/ggge.20056

Cash, J. R., & Karp, A. H. (1990). A variable order Runge-Kutta method for initial value problems with rapidly varying right-hand sides. *ACM Transactions on Mathematical Software (TOMS)*, *16*(3), 201–222. https://doi.org/10.1145/79505.79507

Chen, T., & Lapusta, N. (2009). Scaling of small repeating earthquakes explained by interaction of seismic and aseismic slip in a rate and state fault model. *Journal of Geophysical Research*, *114*, B01311. https://doi.org/10.1029/2008JB005749

Chen, W.-P., & Molnar, P. (1983). Focal depths of intracontinental and intraplate earthquakes and their implications for the thermal and mechanical properties of the lithosphere. *Journal of Geophysical Research*, *88*(B5), 4183–4214. https://doi.org/10.1029/JB088iB05p04183

Chouliaras, G., Pham, V. N., Boyer, D., Bernard, P., & Stavrakakis, G. N. (1997). Crustal structure of the Gulf of Corinth in Central Greece, determined from magnetotelluric soundings. *Annals of Geophysics*, *40*(1). https://doi.org/10.4401/ag-3935

Clément, C., Sachpazi, M., Charvis, P., Graindorge, D., Laigle, M., Hirn, A., & Zafiropoulos, G. (2004). Reflection–refraction seismics in the Gulf of Corinth: Hints at deep structure and control of the deep marine basin. *Tectonophysics*, *391*(1–4), 97–108. https://doi.org/10.1016/j.tecto.2004.07.010

Cowie, P. A., Scholz, C. H., Edwards, M., & Malinverno, A. (1993). Fault strain and seismic coupling on mid-ocean ridges. *Journal of Geophysical Research*, *98*(B10), 17,911–17,920. https://doi.org/10.1029/93JB01567

Deichmann, N. (2006). Local magnitude, a moment revisited. *Bulletin of the Seismological Society of America*, *96*(4A), 1267–1277. https://doi.org/10.1785/0120050115

Deichmann, N. (2017). Theoretical basis for the observed break in ML/M_w scaling between small and large earthquakes. *Bulletin of the Seismological Society of America*, *107*(2), 505–520. https://doi.org/10.1785/0120160318

Dieterich, J. H. (1972). Time-dependent friction in rocks. *Journal of Geophysical Research*, *77*(20), 3690–3697. https://doi.org/10.1029/JB077i020p03690

Dieterich, J. H. (1978). Time-dependent friction and the mechanics of stick-slip. *Pure and Applied Geophysics*, *116*(4–5), 790–806. https://doi.org/10.1007/BF00876539

Dieterich, J. H. (1979). Modeling of rock friction: 1. Experimental results and constitutive equations. *Journal of Geophysical Research*, *84*(B5), 2161–2168. https://doi.org/10.1029/JB084iB05p02161

Dixon, T. H., Jiang, Y., Malservisi, R., McCaffrey, R., Voss, N., Protti, M., & Gonzalez, V. (2014). Earthquake and tsunami forecasts: Relation of slow slip events to subsequent earthquake rupture. *Proceedings of the National Academy of Sciences of the United States of America*, *111*(48), 17,039–17,044. https://doi.org/10.1073/pnas.1412299111

Dodge, D. A., Beroza, G. C., & Ellsworth, W. L. (1996). Detailed observations of California foreshock sequences: Implications for the earthquake initiation process. *Journal of Geophysical Research*, *101*(B10), 22,371–22,392. https://doi.org/10.1029/96JB02269

Dragert, H., Wang, K., & James, T. S. (2001). A silent slip event on the deeper Cascadia subduction interface. *Science*, *292*(5521), 1525–1528. https://doi.org/10.1126/science.1060152

Ebinger, C., Ayele, A., Keir, D., Rowland, J., Yirgu, G., Wright, T., et al. (2010). Length and timescales of rift faulting and magma intrusion: The Afar rifting cycle from 2005 to present. *Annual Review of Earth and Planetary Sciences*, *38*(1), 439–466. https://doi.org/10.1146/annurev-earth-040809-152333

Ekström, G., Nettles, M., & Dziewoński, A. M. (2012). The global CMT project 2004–2010: Centroid-moment tensors for 13,017 earthquakes. *Physics of the Earth and Planetary Interiors*, *200-201*, 1–9. https://doi.org/10.1016/j.pepi.2012.04.002

Ellsworth, W. L., & Beroza, G. C. (1995). Seismic evidence for an earthquake nucleation phase. *Science*, *268*(5212), 851–851, 855. https://doi.org/10.1126/science.268.5212.851

Escartín, J., Cowie, P. A., Searle, R. C., Allerton, S., Mitchell, N. C., MacLeod, C. J., & Slootweg, A. P. (1999). Quantifying tectonic strain and magmatic accretion at a slow spreading ridge segment, mid-Atlantic ridge, 29°N. *Journal of Geophysical Research*, *104*(B5), 10,421–10,437. https://doi.org/10.1029/1998JB900097

Escartín, J., Hirth, G., & Evans, B. (1997). Effects of serpentinization on the lithospheric strength and the style of normal faulting at slow-spreading ridges. *Earth and Planetary Science Letters*, *151*(3-4), 181–189. https://doi.org/10.1016/S0012-821X(97)81847-X

Frohlich, C., & Wetzel, L. R. (2007). Comparison of seismic moment release rates along different types of plate boundaries. *Geophysical Journal International*, *171*(2), 909–920. https://doi.org/10.1111/j.1365-246X.2007.03550.x

Froment, B., McGuire, J. J., van der Hilst, R. D., Gouédard, P., Roland, E. C., Zhang, H., & Collins, J. A. (2014). Imaging along-strike variations in mechanical properties of the Gofar transform fault, East Pacific Rise. *Journal of Geophysical Research: Solid Earth*, *119*, 7175–7194. https://doi.org/10.1002/2014JB011270

Goff, J. A., & Tucholke, B. E. (1997). Multiscale spectral analysis of bathymetry on the flank of the mid-Atlantic ridge: Modification of the seafloor by mass wasting and sedimentation. *Journal of Geophysical Research*, *102*(B7), 15,447–15,462. https://doi.org/10.1029/97JB00723

Hanks, T. C., & Boore, D. M. (1984). Moment-magnitude relations in theory and practice. *Journal of Geophysical Research*, *89*(B7), 6229–6235. https://doi.org/10.1029/JB089iB07p06229

He, C., Wang, Z., & Yao, W. (2007). Frictional sliding of gabbro gouge under hydrothermal conditions. *Tectonophysics*, *445*(3–4), 353–362. https://doi.org/10.1016/j.tecto.2007.09.008

Hirth, G., & Guillot, S. (2013). Rheology and tectonic significance of serpentinite. *Elements*, *9*(2), 107–113. https://doi.org/10.2113/gselements.9.2.107

Houston, H., Delbridge, B. G., Wech, A. G., & Creager, K. C. (2011). Rapid tremor reversals in Cascadia generated by a weakened plate interface. *Nature Geoscience; London*, *4*(6), 404–409. https://doi.org/10.1038/ngeo1157

Howell, S. M., Ito, G., Behn, M. D., Martinez, F., Olive, J.-A., & Escartín, J. (2016). Magmatic and tectonic extension at the Chile Ridge: Evidence for mantle controls on ridge segmentation: Chile Ridge extension and segmentation. *Geochemistry, Geophysics, Geosystems*, *17*, 2354–2373. https://doi.org/10.1002/2016GC006380

International Seismological Centre. (2017). On-line bulletin. Retrieved October 16, 2017, from http://www.isc.ac.uk

Jin, A., Moya, C. A., & Ando, M. (2000). Simultaneous determination of site responses and source parameters of small earthquakes along the Atotsugawa fault zone, Central Japan. *Bulletin of the Seismological Society of America*, *90*(6), 1430–1445. https://doi.org/10.1785/0119990140

Johnson, K. M., Bürgmann, R., & Larson, K. (2006). Frictional properties on the San Andreas fault near Parkfield, California, inferred from models of Afterslip following the 2004 earthquake. *Bulletin of the Seismological Society of America*, *96*(4B), S321–S338. https://doi.org/10.1785/0120050808

Kato, A., Obara, K., Igarashi, T., Tsuruoka, H., Nakagawa, S., & Hirata, N. (2012). Propagation of slow slip leading up to the 2011 M_w 9.0 Tohoku-Oki earthquake. *Science*, *335*(6069), 705–708. https://doi.org/10.1126/science.1215141

Keir, D., Ebinger, C. J., Stuart, G. W., Daly, E., & Ayele, A. (2006). Strain accommodation by magmatism and faulting as rifting proceeds to breakup: Seismicity of the northern Ethiopian rift. *Journal of Geophysical Research*, *111*, B05314. https://doi.org/10.1029/2005JB003748

Lambotte, S., Lyon-Caen, H., Bernard, P., Deschamps, A., Patau, G., Nercessian, A., et al. (2014). Reassessment of the rifting process in the western Corinth rift from relocated seismicity. *Geophysical Journal International*, *197*(3), 1822–1844. https://doi.org/10.1093/gji/ggu096

Lapusta, N., & Liu, Y. (2009). Three-dimensional boundary integral modeling of spontaneous earthquake sequences and aseismic slip. *Journal of Geophysical Research*, *114*, B09303. https://doi.org/10.1029/2008JB005934

Lapusta, N., Rice, J. R., Ben-Zion, Y., & Zheng, G. (2000). Elastodynamic analysis for slow tectonic loading with spontaneous rupture episodes on faults with rate- and state-dependent friction. *Journal of Geophysical Research*, *105*(B10), 23,765–23,789. https://doi.org/10.1029/2000JB900250

Linde, A. T., Gladwin, M. T., Johnston, M. J. S., Gwyther, R. L., & Bilham, R. G. (1996). A slow earthquake sequence on the San Andreas fault. *Nature*, *383*(6595), 65–68. https://doi.org/10.1038/383065a0

Linde, A. T., & Silver, P. G. (1989). Elevation changes and the great 1960 Chilean earthquake: Support for aseismic slip. *Geophysical Research Letters*, *16*(11), 1305–1308. https://doi.org/10.1029/GL016i011p01305

Liu, Y., McGuire, J. J., & Behn, M. D. (2012). Frictional behavior of oceanic transform faults and its influence on earthquake characteristics. *Journal of Geophysical Research*, *117*, B04315. https://doi.org/10.1029/2011JB009025

Liu, Y., & Rice, J. R. (2005). Aseismic slip transients emerge spontaneously in three-dimensional rate and state modeling of subduction earthquake sequences. *Journal of Geophysical Research*, *110*, B08307. https://doi.org/10.1029/2004JB003424

Liu, Y., & Rice, J. R. (2007). Spontaneous and triggered aseismic deformation transients in a subduction fault model. *Journal of Geophysical Research*, *112*, B09404. https://doi.org/10.1029/2007JB004930

Macdonald, K. C., Fox, P. J., Miller, S., Carbotte, S., Edwards, M. H., Eisen, M., et al. (1992). The East Pacific Rise and its flanks 8–18°N: History of segmentation, propagation and spreading direction based on SeaMARC II and sea beam studies. *Marine Geophysical Researches*, *14*(4), 299–344. https://doi.org/10.1007/BF01203621

Macdonald, K. C., Scheirer, D. S., & Carbotte, S. M. (1991). Mid-ocean ridges: Discontinuities, segments and giant cracks. *Science*, *253*(5023), 986–994. https://doi.org/10.1126/science.253.5023.986

Makropoulos, K., Kaviris, G., & Kouskouna, V. (2012). An updated and extended earthquake catalogue for Greece and adjacent areas since 1900. *Natural Hazards and Earth System Sciences*, *12*(5), 1425–1430. https://doi.org/10.5194/nhess-12-1425-2012

Marone, C. (1998). Laboratory-derived friction laws and their application to seismic faulting. *Annual Review of Earth and Planetary Sciences*, *26*(1), 643–696. https://doi.org/10.1146/annurev.earth.26.1.643

Marone, C., & Cox, S. J. D. (1994). Scaling of rock friction constitutive parameters: The effects of surface roughness and cumulative offset on friction of gabbro. *Pure and Applied Geophysics*, *143*(1-3), 359–385. https://doi.org/10.1007/BF00874335

McGuire, J. J. (2008). Seismic cycles and earthquake predictability on East Pacific Rise transform faults. *Bulletin of the Seismological Society of America*, *98*(3), 1067–1084. https://doi.org/10.1785/0120070154

McGuire, J. J., Boettcher, M. S., & Jordan, T. H. (2005). Foreshock sequences and short-term earthquake predictability on East Pacific Rise transform faults. *Nature*, *434*(7032), 457–461. https://doi.org/10.1038/nature03377

McGuire, J. J., Collins, J. A., Gouédard, P., Roland, E., Lizarralde, D., Boettcher, M. S., et al. (2012). Variations in earthquake rupture properties along the Gofar transform fault, East Pacific Rise. *Nature Geoscience*, *5*(5), 336–341. https://doi.org/10.1038/ngeo1454

Mckenzie, D., Jackson, J., & Priestley, K. (2005). Thermal structure of oceanic and continental lithosphere. *Earth and Planetary Science Letters*, *233*(3–4), 337–349. https://doi.org/10.1016/j.epsl.2005.02.005

Métois, M., Socquet, A., & Vigny, C. (2012). Interseismic coupling, segmentation and mechanical behavior of the central Chile subduction zone. *Journal of Geophysical Research*, *117*, B03406. https://doi.org/10.1029/2011JB008736

Micarelli, L., Moretti, I., & Daniel, J. M. (2003). Structural properties of rift-related normal faults: The case study of the Gulf of Corinth, Greece. *Journal of Geodynamics*, *36*(1–2), 275–303. https://doi.org/10.1016/S0264-3707(03)00051-6

Miller, M. M., Melbourne, T., Johnson, D. J., & Sumner, W. Q. (2002). Periodic slow earthquakes from the Cascadia subduction zone. *Science*, *295*(5564), 2423–2423. https://doi.org/10.1126/science.1071193

Montési, L. G. J., & Behn, M. D. (2007). Mantle flow and melting underneath oblique and ultraslow mid-ocean ridges. *Geophysical Research Letters*, *34*, L24307. https://doi.org/10.1029/2007GL031067

Moretti, I., Sakellariou, D., Lykousis, V., & Micarelli, L. (2003). The Gulf of Corinth: An active half graben? *Journal of Geodynamics*, *36*(1–2), 323–340. https://doi.org/10.1016/S0264-3707(03)00053-X

Okada, Y. (1992). Internal deformation due to shear and tensile faults in a half-space. *Bulletin of the Seismological Society of America*, *82*(2), 1018–1040.

Olive, J.-A., & Escartín, J. (2016). Dependence of seismic coupling on normal fault style along the northern mid-Atlantic ridge. *Geochemistry, Geophysics, Geosystems*, *17*, 4128–4152. https://doi.org/10.1002/2016GC006460

Pacheco, J. F., Sykes, L. R., & Scholz, C. H. (1993). Nature of seismic coupling along simple plate boundaries of the subduction type. *Journal of Geophysical Research*, *98*(B8), 14,133–14,159. https://doi.org/10.1029/93JB00349

Papazachos, B. C., Kiratzi, A. A., & Karacostas, B. G. (1997). Toward a homogeneous moment-magnitude determination for earthquakes in Greece and the surrounding area. *Bulletin of the Seismological Society of America*, *87*(2), 474–483.
Peng, Z., & Gomberg, J. (2010). An integrated perspective of the continuum between earthquakes and slow-slip phenomena. *Nature Geoscience*, *3*(9), 599–607. https://doi.org/10.1038/ngeo940
Phipps Morgan, J., Parmentier, E. M., & Lin, J. (1987). Mechanisms for the origin of mid-ocean ridge axial topography: Implications for the thermal and mechanical structure of accreting plate boundaries. *Journal of Geophysical Research*, *92*(B12), 12,823–12,836. https://doi.org/10.1029/JB092iB12p12823
Radiguet, M., Perfettini, H., Cotte, N., Gualandi, A., Valette, B., Kostoglodov, V., et al. (2016). Triggering of the 2014 M_w7.3 Papanoa earthquake by a slow slip event in Guerrero, Mexico. *Nature Geoscience*, *9*(11), 829–833. https://doi.org/10.1038/ngeo2817
Reinen, L. A., Weeks, J. D., & Tullis, T. E. (1991). The frictional behavior of serpentinite: Implications for aseismic creep on shallow crustal faults. *Geophysical Research Letters*, *18*(10), 1921–1924. https://doi.org/10.1029/91GL02367
Reinen, L. A., Weeks, J. D., & Tullis, T. E. (1994). The frictional behavior of lizardite and antigorite serpentinites: Experiments, constitutive models, and implications for natural faults. *Pure and Applied Geophysics*, *143*(1-3), 317–358. https://doi.org/10.1007/BF00874334
Rice, J. R. (1993). Spatio-temporal complexity of slip on a fault. *Journal of Geophysical Research*, *98*(B6), 9885–9907. https://doi.org/10.1029/93JB00191
Rice, J. R., & Ben-Zion, Y. (1996). Slip complexity in earthquake fault models. *Proceedings of the National Academy of Sciences*, *93*(9), 3811–3818. https://doi.org/10.1073/pnas.93.9.3811
Rice, J. R., & Ruina, A. L. (1983). Stability of steady frictional slipping. *Journal of Applied Mechanics*, *50*(2), 343–349. https://doi.org/10.1115/1.3167042
Rigo, A., Lyon-Caen, H., Armijo, R., Deschamps, A., Hatzfeld, D., Makropoulos, K., et al. (1996). A microseismic study in the western part of the Gulf of Corinth (Greece): Implications for large-scale normal faulting mechanisms. *Geophysical Journal International*, *126*(3), 663–688. https://doi.org/10.1111/j.1365-246X.1996.tb04697.x
Roland, E., Lizarralde, D., McGuire, J. J., & Collins, J. A. (2012). Seismic velocity constraints on the material properties that control earthquake behavior at the Quebrada-discovery-Gofar transform faults, East Pacific Rise. *Journal of Geophysical Research*, *117*, B11102. https://doi.org/10.1029/2012JB009422
Rubin, A. M., & Ampuero, J.-P. (2005). Earthquake nucleation on (aging) rate and state faults. *Journal of Geophysical Research*, *110*, B11312. https://doi.org/10.1029/2005JB003686
Ruina, A. (1983). Slip instability and state variable friction laws. *Journal of Geophysical Research*, *88*(B12), 10,359–10,370. https://doi.org/10.1029/JB088iB12p10359
Rundquist, D. V., & Sobolev, P. O. (2002). Seismicity of mid-oceanic ridges and its geodynamic implications: A review. *Earth-Science Reviews*, *58*(1–2), 143–161. https://doi.org/10.1016/S0012-8252(01)00086-1
Scholz, C. H. (1998). Earthquakes and friction laws. *Nature*, *391*(6662), 37–42. https://doi.org/10.1038/34097
Scholz, C. H., & Campos, J. (1995). On the mechanism of seismic decoupling and back arc spreading at subduction zones. *Journal of Geophysical Research*, *100*(B11), 22,103–22,115. https://doi.org/10.1029/95JB01869
Scholz, C. H., & Campos, J. (2012). The seismic coupling of subduction zones revisited. *Journal of Geophysical Research*, *117*, B05310. https://doi.org/10.1029/2011JB009003
Schwartz, S. Y., & Rokosky, J. M. (2007). Slow slip events and seismic tremor at circum-Pacific subduction zones. *Reviews of Geophysics*, *45*, RG3004. https://doi.org/10.1029/2006RG000208
Segall, P., Desmarais, E. K., Shelly, D., Miklius, A., & Cervelli, P. (2006). Earthquakes triggered by silent slip events on Kīlauea volcano, Hawaii. *Nature*, *442*(7098), 71–74. https://doi.org/10.1038/nature04938
Sobolev, P. O., & Rundquist, D. V. (1999). Seismicity of oceanic and continental rifts—A geodynamic approach. *Physics of the Earth and Planetary Interiors*, *111*(3–4), 253–266. https://doi.org/10.1016/S0031-9201(98)00165-4
Solomon, S. C., Huang, P. Y., & Meinke, L. (1988). The seismic moment budget of slowly spreading ridges. *Nature*, *334*(6177), 58–60. https://doi.org/10.1038/334058a0
Stein, C. A., & Stein, S. (1992). A model for the global variation in oceanic depth and heat flow with lithospheric age. *Nature*, *359*(6391), 123–129. https://doi.org/10.1038/359123a0
Taylor, B., Weiss, J. R., Goodliffe, A. M., Sachpazi, M., Laigle, M., & Hirn, A. (2011). The structures, stratigraphy and evolution of the Gulf of Corinth rift, Greece. *Geophysical Journal International*, *185*(3), 1189–1219. https://doi.org/10.1111/j.1365-246X.2011.05014.x
Tichelaar, B. W., & Ruff, L. J. (1993). Depth of seismic coupling along subduction zones. *Journal of Geophysical Research*, *98*(B2), 2017–2037. https://doi.org/10.1029/92JB02045
Tucholke, B. E., Behn, M. D., Buck, W. R., & Lin, J. (2008). Role of melt supply in oceanic detachment faulting and formation of megamullions. *Geology*, *36*(6), 455–458. https://doi.org/10.1130/G24639A.1
Vidale, J. E., & Houston, H. (2012). Slow slip: A new kind of earthquake. *Physics Today*, *65*(1), 38–43. https://doi.org/10.1063/PT.3.1399
Voglis, C., & Lagaris, I. E. (2004). A rectangular trust region dogleg approach for unconstrained and bound constrained nonlinear optimization (p. 7). Presented at the WSEAS.
Wech, A. G., Creager, K. C., & Melbourne, T. I. (2009). Seismic and geodetic constraints on Cascadia slow slip. *Journal of Geophysical Research*, *114*, B10316. https://doi.org/10.1029/2008JB006090
Wiemer, S., & Wyss, M. (2000). Minimum magnitude of completeness in earthquake catalogs: Examples from Alaska, the western United States, and Japan. *Bulletin of the Seismological Society of America*, *90*(4), 859–869. https://doi.org/10.1785/0119990114
Wiens, D. A., & Stein, S. (1984). Intraplate seismicity and stresses in young oceanic lithosphere. *Journal of Geophysical Research*, *89*(B13), 11,442–11,464. https://doi.org/10.1029/JB089iB13p11442
Zelt, B. C., Taylor, B., Sachpazi, M., & Hirn, A. (2005). Crustal velocity and Moho structure beneath the Gulf of Corinth, Greece. *Geophysical Journal International*, *162*(1), 257–268. https://doi.org/10.1111/j.1365-246X.2005.02640.x